

Monolayer puckered pentagonal VTe₂: An emergent two-dimensional ferromagnetic semiconductor with multiferroic coupling

Xuanyi Li¹, Zhili Zhu¹, Qing Yang¹, Zexian Cao¹, Yeliang Wang^{2,1,3}, Sheng Meng¹ (✉), Jiatao Sun^{2,1,4} (✉), and Hongjun Gao^{1,3}

¹ Institute of Physics and University of Chinese Academy of Sciences, Chinese Academy of Sciences, Beijing 100190, China

² School of Information and Electronics, MIIT Key Laboratory for Low-Dimensional Quantum Structure and Devices, Beijing Institute of Technology, Beijing 100081, China

³ CAS Center for Excellence in Topological Quantum Computation, Beijing 100049, China

⁴ BIT Chongqing Center for Microelectronics and Microsystems, Chongqing 401332, China

© Tsinghua University Press and Springer-Verlag GmbH Germany, part of Springer Nature 2021

Received: 7 April 2021 / Revised: 2 June 2021 / Accepted: 16 June 2021

ABSTRACT

Two-dimensional (2D) magnetic crystals have been extensively explored thanks to their potential applications in spintronics, valleytronics, and topological superconductivity. Here we report a novel monolayer magnet, namely puckered pentagonal VTe₂ (PP-VTe₂), intriguing atomic and electronic structures of which were firmly validated from first-principles calculations. The PP-VTe₂ exhibits strong intrinsic ferromagnetism and semiconducting property distinct from the half-metallic bulk pyrite VTe₂ (BP-VTe₂) phase. An unusual magnetic anisotropy with large magnetic exchange energies is found. More interestingly, the multiferroic coupling between its 2D ferroelasticity and in-plane magnetization is further identified in PP-VTe₂, lending it unprecedented controllability with external strains and electric fields. Serving as an emergent 2D ferromagnetic semiconductor with a novel crystal structure, monolayer PP-VTe₂ provides an ideal platform for exploring exotic crystalline and spin configurations in low-dimensional systems.

KEYWORDS

first-principles, puckered pentagonal, VTe₂, ferromagnetic semiconductor, ferroelasticity

1 Introduction

Since the discovery of van der Waals magnetic crystals CrI₃ [1], much research interest has been devoted to exploring the significant potential of two-dimensional (2D) magnets in various fields, such as electronics, spintronics, sensors, information storage, and computing technologies [2–7]. Tremendous studies have been contributed by two aspects of 2D magnetic semiconductors in nanoscale: discovering novel magnetic materials through epitaxial growth, and probing unique magnetic mechanisms through regulating magnetic interactions [8, 9]. Several kinds of 2D materials have been reported to preserve intrinsic 2D ferromagnetism such as Cr₂Ge₂Te₆, Fe₃Ge₂Te₂, CrSe₂, and CrTe₂ [10–13], and both ferromagnetic (FM) and antiferromagnetic (AFM) interlayer interactions, as well as tunable magnetism, have been confirmed in semiconducting CrI₃ and CrBr₃ bilayers [14–17].

Recently, the 2D magnetism had been widely investigated or predicted in vanadium dichalcogenides (VSe₂ and VTe₂) theoretically and experimentally [18–22]. For example, the FM ordering of monolayer VSe₂ on highly oriented pyrolytic graphite and MoS₂ substrates had been reported [18]. However, these results remain debated and the agreement initially reached is that monolayer VSe₂ is not an itinerant magnet since its FM ordering is suppressed by charge density

wave (CDW) [21]. These ambiguous results declare an indecisive conclusion of ferromagnetism in monolayer VSe₂. On the other hand, another vanadium dichalcogenide VTe₂, which was known for the Kondo effect in transport measurements as multilayer nanoplates [23] and a novel (4 × 4) CDW pattern as T-phase monolayer thin films [24–27], haven't been proved to hold any long-range magnetism in previous experiments. With the expectation of magnetism in VTe₂ systems, much effort should be devoted to more phases and their magnetic properties. Besides the traditional T and H phases, there is another unique puckered pentagonal structure for transition metal dichalcogenides, which could be considered as a pyrite structure when thinned to 2D limits represented by layered PdSe₂ [28–30]. To the best of our knowledge, however, the puckered pentagonal phase of VTe₂ (PP-VTe₂) has not been reported, which could have developed magnetism in VTe₂ monolayers.

Here, we report a monolayer puckered pentagonal VTe₂, which is a brand-new phase of vanadium dichalcogenides composed of pentagonal motifs. The structural stability of PP-VTe₂ is dynamically and mechanically confirmed by phonon dispersions and Born–Huang criteria, respectively [31]. The electronic structure calculations indicate an emergent spin-polarized semiconducting band with a 0.33 eV narrow band gap. In-plane FM orderings and high Curie temperature are

Address correspondence to Sheng Meng, smeng@iphy.ac.cn; Jiatao Sun, jtsun@bit.edu.cn



obtained by magnetic exchange energies calculations and Monte Carlo (MC) simulations. Besides the magnetic properties, 2D ferroelastic phase transitions are realized due to the crystal anisotropy induced by lattice distortions and atomic displacements, which further lead to a direct multiferroic coupling. Furthermore, electrical control of magnetism [15] is conceived because of the entire magnetic density of states (DOS) around the Fermi level. Upon that, we proposed that PP-VTe₂ may provide a favorable platform to study the spin-polarized charge carriers' properties and our work will accordingly extend our understanding of 2D semiconducting magnets.

2 Results and discussion

To understand the crystal structures and electronic properties of PP-VTe₂, the bulk VTe₂ with pyrite structure should be firstly investigated. The bulk pyrite phase of VTe₂ (BP-VTe₂) has a space group $Pa\bar{3}$ with a lattice parameter of 6.746 Å. A pentagonal ring in BP-VTe₂ consists of four V–Te bonds of 2.802 Å and one Te–Te bond of 2.865 Å. Puckered pentagonal structural motif extending along two dimensions within the vertical height of 2 Å can be considered as one sub-layer, which is illustrated in Fig. 1(a) with V₂Te₄ per unit cell. The calculated spin-polarized band structure of BP-VTe₂ is shown in Fig. 1(b) with the Brillion zone and high-symmetry momentum paths shown in Fig. 1(d). The BP-VTe₂ shows a half-metallic property, where a metallic band for the spin-up bands and a gap of 1.088 eV for the spin-down bands are obtained. Each V has 6 nearest Te neighbors forming an octahedral crystal field, further leading to the split of e_g and t_{2g} levels, where the three low t_{2g} levels are occupied by the 3 unpaired electrons indicating a large magnetic moment of 3 μ_B per V atom. The chemical formation energy of BP-VTe₂ is -0.265 eV per atom, which is only a little higher than that of the well-known VTe₂ phases such as 1T-VTe₂ (-0.307 eV), indicating the potential to be synthesized in experiments.

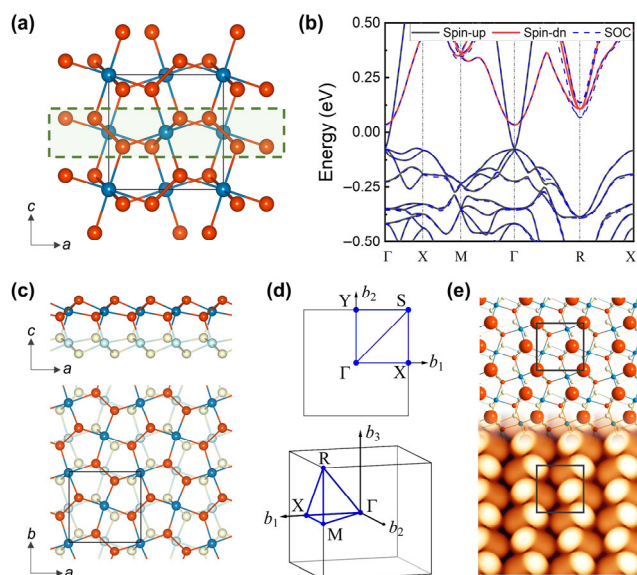


Figure 1 (a) Crystal structure of the BP-VTe₂, where one sub-layer of V₂Te₄ in its unit cell is denoted by the green dashed lines. (b) Band structures of the BP-VTe₂ with and without SOC. (c) Top and side views of the PP-VTe₂. (d) The Brillion zone and high-symmetry momentum paths of PP-VTe₂ (upper panel) and BP-VTe₂ (lower panel). (e) A structural model (upper panel) and its corresponding simulated STM topography (lower panel) of the PP-VTe₂, where topmost Te atoms have been highlighted as large spheres. In this figure, all spheres of deep-blue and light-cyan represent V atoms and all spheres of orange-red and light-yellow represent Te atoms. Unit cells are circled by black lines.

Figure 1(c) displays the atomic structure of monolayer PP-VTe₂ with the side view and top view. We find that there are two sub-layers chemically bonded with each other in the PP-VTe₂ monolayer but only one independent sub-layer can not stay stable. The space group of the PP-VTe₂ is $Pca2_1$. Symmetry operations are reduced compared with those of the BP-VTe₂ because of lattice distortions accompanying atomic displacements. Therefore, the structural shape of PP-VTe₂ becomes rectangular with a cell parameter $a = 6.774$ Å and $b = 6.655$ Å, leading to the opportunity for 2D ferroelasticity. Moreover, in pentagonal motifs, the nearest distance between V and Te from different sub-layers is shorter than all of the bond lengths inside one sub-layer, indicating strong bonding energy between these two sub-layers as analogous to PdSe₂ thin films [32, 33]. Figure 1(e) shows a monolayer structural model with its corresponding simulated image of scanning tunneling microscope (STM) under the bias of -0.5 eV. The brightest signals correspond to the topmost Te atoms of the buckling top sub-layer, indicating that a zigzag-like pattern will be observed under certain experimental conditions.

In order to confirm the structural stability of the monolayer PP-VTe₂, linear elastic constants and phonon dispersions were calculated. The calculated elastic constants of PP-VTe₂ are listed as: $C_{11} = 49.66$ N/m, $C_{22} = 72.92$ N/m; $C_{12} = 6.976$ N/m; $C_{44} = 24.59$ N/m (z -axis is perpendicular to the VTe₂ plane). It can be found that these elastic parameters satisfy the Born–Huang criteria, $C_{11}C_{22} - C_{12}^2 > 0$, $C_{44} > 0$, indicating the mechanical stability of the PP-VTe₂. The calculated phonon dispersions are shown in Fig. 2(a). There is no imaginary frequency in the whole Brillion zone, indicating that the PP-VTe₂ is dynamically stable. To study if there are certain layer slidings or displacements, we calculated the total energy by manually sliding each sub-layer. Figure 2(b) shows the calculated relative total energy of the monolayer PP-VTe₂ with different relative displacements between two sub-layers. These calculations demonstrate that the monolayer PP-VTe₂ system has the

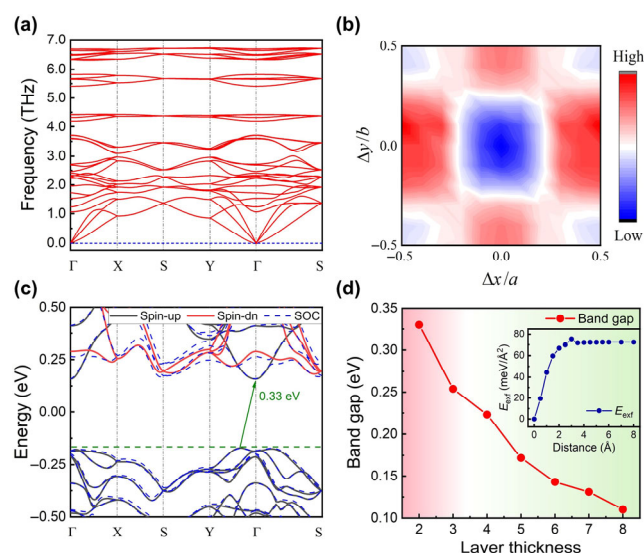


Figure 2 (a) The calculated phonon dispersions of the monolayer PP-VTe₂. (b) The relative total energy with different relative displacements between two sub-layers. The coordinate value represents the ratio of the sliding length to the cell parameters. (c) Band structures of the PP-VTe₂ with and without SOC. A 0.33 eV band gap is illustrated. (d) The gradual reduction of the band gap with the increase of the layer thickness of the PP-VTe₂ slab. The coordinate value represents the number of sub-layers. The pink and light-green backgrounds denote the regions of indirect and direct band gap depending on the layer thickness. The inset shows the calculated exfoliation energy of PP-VTe₂.

lowest energy when these two sub-layers don't have any relative displacement (the case in Fig. 1(c)). Besides, as shown in the inset of Fig. 2(d), the exfoliation energy of $72.46 \text{ meV}/\text{\AA}^2$ is needed from BP-VTe₂ to PP-VTe₂. Thanks to the decreased exfoliation energy, we propose that PP-VTe₂ has a great possibility to be realized [34] through epitaxial growth like the PdSe₂ monolayers.

The calculated band structures of the PP-VTe₂ are displayed in Fig. 2(c) along high symmetry momentum paths in Fig. 1(d). It is revealed that the monolayer PP-VTe₂ is a magnetic semiconductor with an indirect band gap of 0.33 eV, which shows great distinction from the half-metallic band structure of the BP-VTe₂ in Fig. 1(b). When the thickness of the 2D PP-VTe₂ slab increases, the band gap of the slab will decrease from 0.33 eV (2 sub-layers) to 0.11 eV (8 sub-layers) accompanying the indirect to direct transition as shown in Fig. 2(d), which gradually reflects the electronic property of the bulk phase. It is worth noting that the tunable band gap from 0.33 to 0.11 eV is smaller than the hitherto reported 2D magnetic semiconductors like CrI₃ (1.07 eV), CrBr₃ (1.34 eV), and Cr₂Ge₂Te₆ (0.88 eV at HSE level [35]). Therefore, PP-VTe₂ is an unusual 2D narrow-gap ferromagnetic semiconductor aiming for infrared optoelectronics.

In order to figure out the magnetic ground states of the PP-VTe₂ system, the magnetic exchange energies were calculated at different magnetic states including nonmagnetic (NM), FM, and three AFM states without the inclusion of spin-orbit coupling (SOC). Possible magnetic configurations of the monolayer PP-VTe₂ are shown in Fig. S1(a) in the Electronic Supplementary Material (ESM). In our calculations, by changing the on-site Coulomb (U) and exchange interactions (J) as in the Dudarev method [36], the density functional theory (DFT) + U approach was performed for V 3d orbitals to study the effect of electron Coulomb interaction U_{eff} (the difference between U and J). Different effective Hubbard energy U_{eff} values as 0, 3, and 5 eV have been considered. Figure S1(b) in the ESM shows the relative total energies per unit cell of the various magnetic states for PP-VTe₂, where the total energy of the FM state is taken as a reference under any different U_{eff} . We find that the overall relative total energies of the NM and AFM states are positive and much higher than that of the FM state, which means that monolayer PP-VTe₂ is an intrinsic ferromagnetic semiconductor.

With the intrinsic FM ordering nature, the easy-magnetization axis of the monolayer PP-VTe₂ is obtained by calculating magnetic anisotropy energy (MAE). According to Fig. 3(a), when rotating the spin orientations and calculating the total energies inside the x - y plane, the lowest energy state corresponds to the M_a [100] direction with respect to the in-plane M_b [010] and M_c [110] directions by 0.45 and 1.83 meV, as well as the out-of-plane M_c [001] direction by 1.23 meV per unit cell. After examining the MAE from in-plane to out-of-plane orientations, we conclude that the in-plane magnetization shown in Fig. 3(b), which exactly coincides with the orientation of the only screw axis of PP-VTe₂ along the x -axis, is energetically preferred because of the inherent crystal symmetry. Besides, several energy local minimums at symmetrical angles are found in Fig. 3(a) corresponding with the directions of V-Te chemical bonds. Therefore, we further set the magnetic moment vectors approaching the orientations of each V-Te bond as inclined-FM states, one of which is shown in Fig. 3(c). Because of the different chemical environments for each V atom, the total energy of the inclined-FM state is a little higher than that of the in-plane FM state in Fig. 3(b) by 0.15 meV, which can be

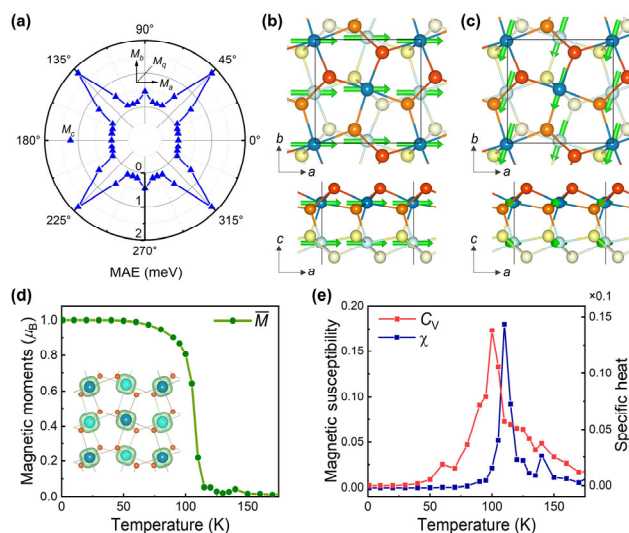


Figure 3 (a) MAE by rotating the spin orientations within the x - y plane of the PP-VTe₂, where the calculated relative total energies at certain degrees are marked as blue triangles. The relative energy of M_a [100] is set to be zero. (b) The energetically preferred magnetic state of the PP-VTe₂. (c) An inclined-FM state, where the orientation of magnetic moments corresponds to the direction of one V-Te chemical bond. (d) The simulated average magnetic moments as a dependence of temperature. The inset is the spin density for PP-VTe₂. The isosurface value for spin density is $0.17 \text{ e}/\text{\AA}^3$. (e) The simulated magnetic susceptibility χ and specific heat C_V as a dependence of temperature. In this figure, all spheres of deep-blue and light-cyan represent V atoms from the upper and lower sub-layer, respectively. The other spheres represent Te atoms.

considered as a metastable magnetic state determined by the puckered pentagonal motifs.

To estimate the Curie temperature for the FM PP-VTe₂ monolayer, we conducted MC simulations based on a quasi-2D Heisenberg model concerning the specific lattice with two sub-layers. There are eight nearest magnetic atom neighbors for each vanadium, where four of them are located at the same sub-layer and the other four are located at another sub-layer as shown in the inset of Fig. 3(d). We consider the nearest neighbor spin-exchange interaction and ion anisotropy in the Hamiltonian of the Heisenberg model [37]

$$H = \sum_{\langle i,j \rangle} J_0 \mathbf{S}_i \cdot \mathbf{S}_j + \sum_i \lambda \mathbf{S}_i^2 \quad (1)$$

Here, $J_0 = 3.68 \text{ meV}$ obtained by the magnetic exchange energy represents the nearest coupling of PP-VTe₂ [38] and λ describes the easy axis single-ion anisotropy obtained by MAE. Based on the Hamiltonian above, MC simulations were conducted on a 2D mesh grids of 100×100 . The simulations lasted for 5,000,000 steps with a temperature step of 5 K. The magnetic susceptibility, $\chi = \frac{\partial M}{\partial H} = \frac{\text{Var}(M)}{T}$, and the specific heat, $C_V = \frac{\partial U}{\partial T} = \frac{\text{Var}(E)}{T^2}$, were both considered through the MC simulations simultaneously, where E means the total energy of our quasi-2D lattice. As revealed by Figs. 3(d) and 3(e), we estimate the Curie temperature of PP-VTe₂ as 110 K, which is comparable with the experimentally realized 2D magnetic semiconductors such as CrI₃ (45 K), CrBr₃ (27 K), and Cr₂Ge₂Te₆ (30 K) [39], and other theoretically proposed 2D magnetic materials [40–43] or organometallic lattices [44].

Due to the lack of four-fold rotational symmetry, the monolayer PP-VTe₂ exhibits the crystal anisotropy of 1.8% between in-plane lattice parameters a and b promising for

2D ferroelasticity. Then the relative energies as a function of the phase transition pathway were calculated, and the energy barriers of ferroelastic switching were estimated by using the nudged elastic band (NEB) theory [45]. To constrain the unit cell and reduce the influence of lattice deformation during the switching procedures, we firstly applied a compressive strain along the x -axis and a tensile strain along the y -axis on the initial state (IS) in Fig. 4(a) to transform the rectangular lattice into a square one. By rotating the IS for 90° , the lattice of the final state (FS) was obtained and shown in Figs. 4(c) and 4(e). Considering that atomic positions between the IS and FS are different, an intermediate state (MS) is proposed as shown in Fig. 4(b). Comparing the MS with the IS, all Te atoms in the lower sub-layer move horizontally maintaining the puckered pentagonal motif intact. The transition switches from the IS to the FS via the MS, leading to an overall energy barrier of 258 meV per atom as shown in Fig. 4(d), which is comparable with the 2D nonmagnetic ferroelastic material black phosphorene [46]. Such small strains of 1.8% driving the ferroelastic phase transitions of PP-VTe₂ can be feasibly realized. In particular, a 90° rotation of the easy-magnetization axis will be observed after the occurrence of ferroelastic phase transitions, indicating a direct 2D multiferroic coupling between the ferroelasticity and in-plane magnetization controlled by external strains in PP-VTe₂ monolayer.

Based on the calculated spin-polarized band structure (Fig. S2(a) in the ESM) and projected DOS (Fig. S2(b) in the ESM) of the monolayer PP-VTe₂, we find out that the total magnetic moments completely arise from the spin-polarized states ranging from -1 to -0.1 eV, which are almost donated by the V 3d electrons as indicated by the blue shadows. As a ferromagnetic semiconductor, when the chemical potential (relative to the Fermi level) is tuned through gating voltage, the electron occupation of the spin-up bands will be changed with respect to the spin-down bands. Consequently, the net magnetic moment of the PP-VTe₂ sample can be tuned from 12 to $10 \mu_B$ per unit cell under a hole concentration of 4.5×10^{14} per squared centimeter, indicating that monolayer PP-VTe₂ is a great candidate for electrical control of magnetism on a high-dielectric substrate [47], which is schematically shown in Fig. S2(c) in the ESM. Owing to the similar band structure near the Fermi level of PP-VSe₂ and PP-VS₂ with PP-VTe₂ (Fig. S3 in the ESM), the electrical

control of magnetism is promising to be realized in the puckered pentagonal structures of VSe₂ and VS₂ as well.

3 Conclusions

We have predicted an emergent ferromagnetic semiconductor of monolayer VTe₂ with a 2D puckered pentagonal configuration that is dynamically stable. Distinct from the half-metallic BP-VTe₂ and other conventional 2D semiconducting magnets, we show that PP-VTe₂ is a narrow-gap semiconductor proposed for infrared optoelectronics. The FM ground state with unusual in-plane magnetic anisotropy and the estimated Curie temperature as 110 K of PP-VTe₂ are demonstrated. The 2D multiferroic coupling that ferroelastic phase transitions will lead to the switching of the easy-magnetization axis in PP-VTe₂ has also been explained by its exotic crystal structures. Moreover, we notice a feasible electrical control of magnetism in PP-VTe₂ since its magnetic DOS completely arises from the spin-polarized states near the Fermi level. In a word, as a 2D semiconductor with a unique crystal structure and strong ferromagnetism, monolayer PP-VTe₂ is an ideal 2D material for studying magnetic and ferroelastic properties, as well as tunable states by external strains and electric fields.

4 Methods

The DFT calculations were implemented by Vienna *ab initio* simulation package (VASP) [48]. Ion cores and wave functions were described by the projector augmented wave (PAW) [49] method. All structural relaxations were conducted by using the generalized gradient approximation (GGA) proposed by Perdew, Burke, and Ernzerhof (PBE) [50], with a $9 \times 9 \times 1$ k -point grid generated by Monkhost-Pack. High-precision geometry relaxation would stop only when the total energy difference was less than 10^{-8} eV and Hellmann-Feynman forces were less than 10^{-6} eV/Å, which is critical for annihilating the imaginary phonon modes. The plane-wave cutoff energy was set to be 500 eV. A vacuum space of 20 Å was adopted. The phonon dispersions were obtained by density functional perturbation theory (DFPT). The finite distortion method [51] was used when we calculated the linear elastic constants. Additionally, SOC was included in self-consistent calculations when calculating the MAE.

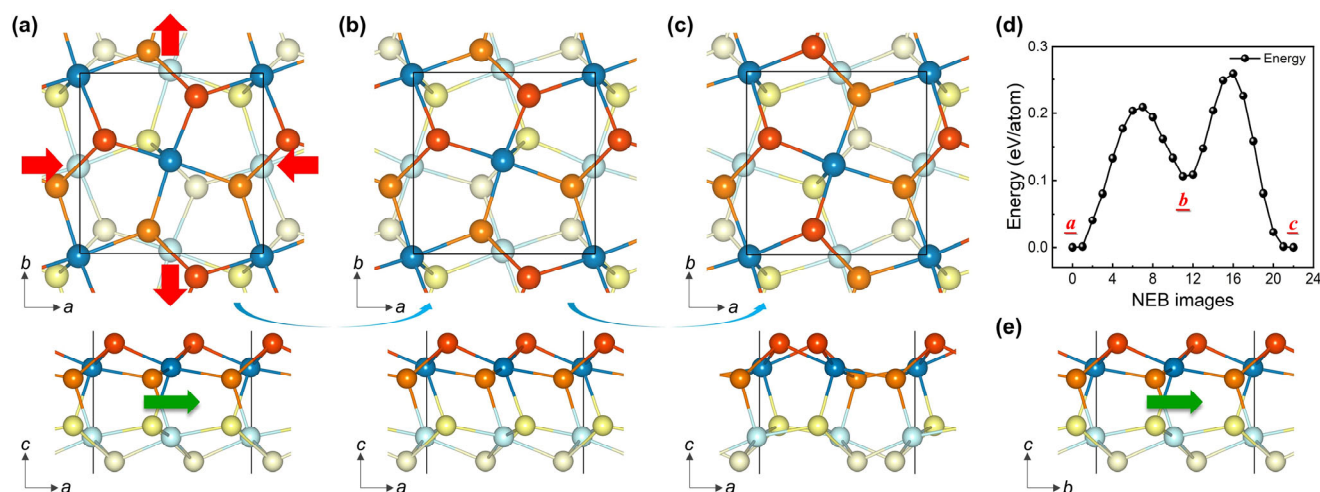


Figure 4 Pathway for the ferroelastic switching from the (a) initial state via the (b) intermediate state to the (c) final state. (d) The total energy as a function of NEB images during the ferroelastic phase transitions. Three representative states are marked. (e) Another side view of the final state, which is same as the side view of the initial state in (a) indicating a successful ferroelastic switching. In this figure, deep-blue and light-cyan spheres represent V atoms from the upper and lower sub-layer, respectively. The other spheres represent Te atoms. Red arrows denote the compressive or tensile strains. Green arrows denote the direction of the easy-magnetization axis. Blue arrows denote the switching procedures.

Acknowledgements

This work was financially supported by the National Key Research and Development Program of China (Nos. 2020YFA0308800, 2016YFA0202300, and 2016YFA0300902), the National Natural Science Foundation of China (Nos. 91850120 and 11974045), and the Strategic Priority Research Program (B) of CAS (No. XDB30000000). The computing resources were provided by the Institute of Physics, Chinese Academy of Sciences and Songshan Lake Supercomputing Facilities.

Electronic Supplementary Material: Supplementary material (Magnetic configurations and electrical control of magnetism of the PP-VTe₂, band structures of PP-VSe₂ and PP-VS₂, and atomic structures of BP- and PP-VTe₂) is available in the online version of this article at <https://doi.org/10.1007/s12274-021-3692-5>.

References

- Huang, B.; Clark, G.; Navarro-Moratalla, E.; Klein, D. R.; Cheng, R.; Seyler, K. L.; Zhong, D.; Schmidgall, E.; McGuire, M. A.; Cobden, D. H. et al. Layer-dependent ferromagnetism in a van der Waals crystal down to the monolayer limit. *Nature* **2017**, *546*, 270–273.
- Avsar, A.; Ochoa, H.; Guinea, F.; Özyilmaz, B.; van Wees, B. J.; Vera-Marun, I. J. *Colloquium: Spintronics in graphene and other two-dimensional materials*. *Rev. Mod. Phys.* **2020**, *92*, 021003.
- Lin, X. Y.; Yang, W.; Wang, K. L.; Zhao, W. S. Two-dimensional spintronics for low-power electronics. *Nat. Electron.* **2019**, *2*, 274–283.
- Gibertini, M.; Koperski, M.; Morpurgo, A. F.; Novoselov, K. S. Magnetic 2D materials and heterostructures. *Nat. Nanotechnol.* **2019**, *14*, 408–419.
- Jimenez, V. O.; Kalappattil, V.; Eggers, T.; Bonilla, M.; Kolekar, S.; Huy, P. T.; Batzill, M.; Phan, M. H. A magnetic sensor using a 2D van der Waals ferromagnetic material. *Sci. Rep.* **2020**, *10*, 4789.
- Shen, J. X.; Shang, D. S.; Chai, Y. S.; Wang, S. G.; Shen, B. G.; Sun, Y. Mimicking synaptic plasticity and neural network using memtransistors. *Adv. Mater.* **2018**, *30*, 1706717.
- Liu, C. S.; Chen, H. W.; Wang, S. Y.; Liu, Q.; Jiang, Y. G.; Zhang, D. W.; Liu, M.; Zhou, P. Two-dimensional materials for next-generation computing technologies. *Nat. Nanotechnol.* **2020**, *15*, 545–557.
- Gong, C.; Zhang, X. Two-dimensional magnetic crystals and emergent heterostructure devices. *Science* **2019**, *363*, eaav4450.
- Mak, K. F.; Shan, J.; Ralph, D. C. Probing and controlling magnetic states in 2D layered magnetic materials. *Nat. Rev. Phys.* **2019**, *1*, 646–661.
- Gong, C.; Li, L.; Li, Z. L.; Ji, H. W.; Stern, A.; Xia, Y.; Cao, T.; Bao, W.; Wang, C. Z.; Wang, Y. et al. Discovery of intrinsic ferromagnetism in two-dimensional van der Waals crystals. *Nature* **2017**, *546*, 265–269.
- Deng, Y. J.; Yu, Y. J.; Song, Y. C.; Zhang, J. Z.; Wang, N. Z.; Sun, Z. Y.; Yi, Y. F.; Wu, Y. Z.; Wu, S. W.; Zhu, J. Y. et al. Gate-tunable room-temperature ferromagnetism in two-dimensional Fe₃GeTe₂. *Nature* **2018**, *563*, 94–99.
- Li, B.; Wan, Z.; Wang, C.; Chen, P.; Huang, B.; Cheng, X.; Qian, Q.; Li, J.; Zhang, Z. W.; Sun, G. Z. et al. Van der Waals epitaxial growth of air-stable CrSe₂ nanosheets with thickness-tunable magnetic order. *Nat. Mater.* **2021**, *20*, 818–825.
- Sun, X. D.; Li, W. Y.; Wang, X.; Sui, Q.; Zhang, T. Y.; Wang, Z.; Liu, L.; Li, D.; Feng, S.; Zhong, S. Y. et al. Room temperature ferromagnetism in ultra-thin van der Waals crystals of 1T-CrTe₂. *Nano Res.* **2020**, *13*, 3358–3363.
- Thiel, L.; Wang, Z.; Tschudin, M. A.; Rohner, D.; Gutiérrez- Lezama, I.; Ubrig, N.; Gibertini, M.; Giannini, E.; Morpurgo, A. F.; Maletinsky, P. Probing magnetism in 2D materials at the nanoscale with single-spin microscopy. *Science* **2019**, *364*, 973–976.
- Huang, B.; Clark, G.; Klein, D. R.; MacNeill, D.; Navarro-Moratalla, E.; Seyler, K. L.; Wilson, N.; McGuire, M. A.; Cobden, D. H.; Xiao, D. et al. Electrical control of 2D magnetism in bilayer CrI₃. *Nat. Nanotechnol.* **2018**, *13*, 544–548.
- Jiang, S. W.; Li, L. Z.; Wang, Z. F.; Mak, K. F.; Shan, J. Controlling magnetism in 2D CrI₃ by electrostatic doping. *Nat. Nanotechnol.* **2018**, *13*, 549–553.
- Chen, W. J.; Sun, Z. Y.; Wang, Z. J.; Gu, L. H.; Xu, X. D.; Wu, S. W.; Gao, C. L. Direct observation of van der Waals stacking-dependent interlayer magnetism. *Science* **2019**, *366*, 983–987.
- Bonilla, M.; Kolekar, S.; Ma, Y. J.; Diaz, H. C.; Kalappattil, V.; Das, R.; Eggers, T.; Gutierrez, H. R.; Phan, M. H.; Batzill, M. Strong room-temperature ferromagnetism in VSe₂ monolayers on van der Waals substrates. *Nat. Nanotechnol.* **2018**, *13*, 289–293.
- Liu, Z. L.; Wu, X.; Shao, Y.; Qi, J.; Cao, Y.; Huang, L.; Liu, C.; Wang, J. O.; Zheng, Q.; Zhu, Z. L. et al. Epitaxially grown monolayer VSe₂: An air-stable magnetic two-dimensional material with low work function at edges. *Sci. Bull.* **2018**, *63*, 419–425.
- Yu, W.; Li, J.; Herng, T. S.; Wang, Z. S.; Zhao, X. X.; Chi, X.; Fu, W.; Abdelwahab, I.; Zhou, J.; Dan, J. D. et al. Chemically exfoliated VSe₂ monolayers with room-temperature ferromagnetism. *Adv. Mater.* **2019**, *31*, 1903779.
- Coelho, P. M.; Nguyen Cong, K.; Bonilla, M.; Kolekar, S.; Phan, M. H.; Avila, J.; Asensio, M. C.; Oleynik, I. I.; Batzill, M. Charge density wave state suppresses ferromagnetic ordering in VSe₂ monolayers. *J. Phys. Chem. C* **2019**, *123*, 14089–14096.
- Zhang, W.; Zhang, L.; Wong, P. K. J.; Yuan, J. R.; Vinai, G.; Torelli, P.; van der Laan, G.; Feng, Y. P.; Wee, A. T. S. Magnetic transition in monolayer VSe₂ via interface hybridization. *ACS Nano* **2019**, *13*, 8997–9004.
- Liu, H. T.; Xue, Y. Z.; Shi, J. A.; Guzman, R. A.; Zhang, P. P.; Zhou, Z.; He, Y. G.; Bian, C.; Wu, L. M.; Ma, R. S. et al. Observation of the kondo effect in multilayer single-crystalline VTe₂ nanoplates. *Nano Lett.* **2019**, *19*, 8572–8580.
- Liu, M. Z.; Wu, C. W.; Liu, Z. Z.; Wang, Z. Q.; Yao, D. X.; Zhong, D. Y. Multimorphism and gap opening of charge-density-wave phases in monolayer VTe₂. *Nano Res.* **2020**, *13*, 1733–1738.
- Coelho, P. M.; Lasek, K.; Nguyen Cong, K.; Li, J. F.; Niu, W.; Liu, W. Q.; Oleynik, I. I.; Batzill, M. Monolayer modification of VTe₂ and its charge density wave. *J. Phys. Chem. Lett.* **2019**, *10*, 4987–4993.
- Wang, Y.; Ren, J. H.; Li, J. H.; Wang, Y. J.; Peng, H. N.; Yu, P.; Duan, W. H.; Zhou, S. Y. Evidence of charge density wave with anisotropic gap in a monolayer VTe₂ film. *Phys. Rev. B* **2019**, *100*, 241404(R).
- Miao, G. Y.; Xue, S. W.; Li, B.; Lin, Z. J.; Liu, B.; Zhu, X. T.; Wang, W. H.; Guo, J. D. Real-space investigation of the charge density wave in VTe₂ monolayer with broken rotational and mirror symmetries. *Phys. Rev. B* **2020**, *101*, 035407.
- Oyedele, A. D.; Yang, S. Z.; Liang, L. B.; Puzetky, A. A.; Wang, K.; Zhang, J. J.; Yu, P.; Pudasaini, P. R.; Ghosh, A. W.; Liu, Z. et al. PdSe₂: Pentagonal two-dimensional layers with high air stability for electronics. *J. Am. Chem. Soc.* **2017**, *139*, 14090–14097.
- Li, E.; Wang, D. F.; Fan, P.; Zhang, R. Z.; Zhang, Y. Y.; Li, G.; Mao, J. H.; Wang, Y. L.; Lin, X.; Du, S. X. et al. Construction of bilayer PdSe₂ on epitaxial graphene. *Nano Res.* **2018**, *11*, 5858–5865.
- Lu, L. S.; Chen, G. H.; Cheng, H. Y.; Chuu, C. P.; Lu, K. C.; Chen, C. H.; Lu, M. Y.; Chuang, T. H.; Wei, D. H.; Chueh, W. C. et al. Layer-dependent and in-plane anisotropic properties of low-temperature synthesized few-layer PdSe₂ single crystals. *ACS Nano* **2020**, *14*, 4963–4972.
- Born, M.; Huang, K. *Dynamical Theory of Crystal Lattices*; Oxford University Press: Oxford, UK, 1954.
- Lin, J. H.; Zuluaga, S.; Yu, P.; Liu, Z.; Pantelides, S. T.; Suenaga, K. Novel Pd₂Se₃ Two-dimensional phase driven by interlayer fusion in layered PdSe₂. *Phys. Rev. Lett.* **2017**, *119*, 016101.
- Puzetky, A. A.; Oyedele, A. D.; Xiao, K.; Haglund, A. V.; Sumpter, B. G.; Mandrus, D.; Geohagan, D. B.; Liang, L. B. Anomalous interlayer vibrations in strongly coupled layered PdSe₂. *2D Mater.* **2018**, *5*, 035016.
- Mounet, N.; Gibertini, M.; Schwaller, P.; Campi, D.; Merkys, A.; Marrazzo, A.; Sohier, T.; Castelli, I. E.; Cepellotti, A.; Pizzi, G. et al. Two-dimensional materials from high-throughput computational exfoliation of experimentally known compounds. *Nat. Nanotechnol.* **2018**, *13*, 246–252.

- [35] Li, X. X.; Yang, J. L. CrXTe₃ (X = Si, Ge) Nanosheets: Two dimensional intrinsic ferromagnetic semiconductors. *J. Mater. Chem. C* **2014**, *2*, 7071–7076.
- [36] Lutfalla, S.; Shapovalov, V.; Bell, A. T. Calibration of the DFT/GGA+U Method for determination of reduction energies for transition and rare earth metal oxides of Ti, V, Mo, and Ce. *J. Chem. Theory Comput.* **2011**, *7*, 2218–2223.
- [37] Li, X. Y.; Meng, S.; Sun, J. T. Emergence of *d*-orbital magnetic dirac fermions in a MoS₂ monolayer with squared pentagon structure. *Phys. Rev. B* **2020**, *101*, 144409.
- [38] Zhu, Y.; Kong, X. H.; Rhone, T. D.; Guo, H. Systematic search for two-dimensional ferromagnetic materials. *Phys. Rev. Mater.* **2018**, *2*, 081001(R).
- [39] Lu, X. B.; Fei, R. X.; Yang, L. Curie temperature of emerging two-dimensional magnetic structures. *Phys. Rev. B* **2019**, *100*, 205409.
- [40] Wang, C.; Zhou, X. Y.; Zhou, L. W.; Tong, N. H.; Lu, Z. Y.; Ji, W. A family of high-temperature ferromagnetic monolayers with locked spin-dichroism-mobility anisotropy: MnNX and CrCX (X = Cl, Br, I; C = S, Se, Te). *Sci. Bull.* **2019**, *64*, 293–300.
- [41] Sun, Y. J.; Zhuo, Z. W.; Wu, X. J. Bipolar magnetism in a two-dimensional NbS₂ semiconductor with high curie temperature. *J. Mater. Chem. C* **2018**, *6*, 11401–11406.
- [42] Jiang, Z.; Wang, P.; Xing, J. P.; Jiang, X.; Zhao, J. J. Screening and design of novel 2D ferromagnetic materials with high curie temperature above room temperature. *ACS Appl. Mater. Interfaces* **2018**, *10*, 39032–39039.
- [43] Guo, Y. L.; Wang, B.; Zhang, X. W.; Yuan, S. J.; Ma, L.; Wang, J. L. Magnetic two-dimensional layered crystals meet with ferromagnetic semiconductors. *InfoMat* **2020**, *2*, 639–655.
- [44] Li, X. X.; Yang, J. L. Toward room-temperature magnetic semiconductors in two-dimensional ferrimagnetic organometallic lattices. *J. Phys. Chem. Lett.* **2019**, *10*, 2439–2444.
- [45] Henkelman, G.; Uberuaga, B. P.; Jónsson, H. Climbing image nudged elastic band method for finding saddle points and minimum energy paths. *J. Chem. Phys.* **2000**, *113*, 9901–9904.
- [46] Wu, M. H.; Zeng, X. C. Intrinsic ferroelasticity and/or multiferroicity in two-dimensional phosphorene and phosphorene analogues. *Nano Lett.* **2016**, *16*, 3236–3241.
- [47] Zhang, G. H.; Qin, H. J.; Chen, J.; He, X. Y.; Lu, L.; Li, Y. Q.; Wu, K. H. Growth of topological insulator Bi₂Se₃ thin films on SrTiO₃ with large tunability in chemical potential. *Adv. Funct. Mater.* **2011**, *21*, 2351–2355.
- [48] Kresse, G.; Furthmüller, J. Efficient iterative schemes for *ab initio* total-energy calculations using a plane-wave basis set. *Phys. Rev. B* **1996**, *54*, 11169–11186.
- [49] Blöchl, P. E. Projector augmented-wave method. *Phys. Rev. B* **1994**, *50*, 17953–17979.
- [50] Perdew, J. P.; Burke, K.; Ernzerhof, M. Generalized gradient approximation made simple. *Phys. Rev. Lett.* **1996**, *77*, 3865–3868.
- [51] Le Page, Y.; Saxe, P. Symmetry-general least-squares extraction of elastic data for strained materials from *ab initio* calculations of stress. *Phys. Rev. B* **2002**, *65*, 104104.